

REPORT DOCUMENTATION PAGE

1. REPORT SECURITY CLASSIFICATION Unclassified	16. RESTRICTIVE MARKINGS		
2. SECURITY CLASSIFICATION AUTHORITY 1	3. DISTRIBUTION/AVAILABILITY OF REPORT		
4. DECLASSIFICATION/DOWNGRADING SCHEDULE			
5. PERFORMING ORGANIZATION REPORT NUMBER(S) N96-13		5. MONITORING ORGANIZATION REPORT NUMBER(S) N00014-93-1-0109; N00014-96-1-0110	
6. NAME OF PERFORMING ORGANIZATION Arizona State University	7b. OFFICE SYMBOL <i>(If applicable)</i>	7a. NAME OF MONITORING ORGANIZATION Office of Naval Research	
8c. ADDRESS (City, State and ZIP Code) Center for Solid State Electronics Res. Tempe, AZ 85287-6206		7b. ADDRESS (City, State and ZIP Code) 800 N. Quincy Street Arlington, VA 22217	
9a. NAME OF FUNDING/SPONSORING ORGANIZATION Office of Naval Research	8b. OFFICE SYMBOL <i>(If applicable)</i>	9. PROCUREMENT INSTRUMENT IDENTIFICATION NUMBER	
10. ADDRESS (City, State and ZIP Code) 800 N. Quincy Street Arlington, VA 22217		10. SOURCE OF FUNDING NOS	
		PROGRAM ELEMENT NO.	PROJECT NO.
			TASK NO.
			WORK UNIT NO.
11. TITLE <i>(Include Security Classification)</i> (See Reverse Side)		14. DATE OF REPORT (Year, Month, Day) 9/11/96	
12. PERSONAL AUTHORITY D. Vasileska, T. Eldridge, and D.K. Ferry		15. PAGE COUNT 6	
13a. TYPE OF REPORT Reprint	13b. TIME COVERED FROM _____ TO _____	13c. SUBJECT TERMS <i>(Continue on reverse if necessary and identify by block number)</i> Quantum transport; Semiconductors; Green's functions	
16. SUPPLEMENTARY NOTATION			
17. ABSTRACT <i>(Continue on reverse if necessary and identify by block number)</i> Using a real-time Green's functions formalism, we investigate the influence of depletion charge scattering on the room temperature mobility in scaled silicon metal-oxide-semiconductor field-effect transistors and low-temperature transport in In _{0.4} Al _{0.6} As-In _{0.4} Ga _{0.6} As modulation doped heterostructures. Our simulation results suggest that depletion charge scattering, which is usually ignored, has considerable impact on the electron transport in silicon inversion layers near the threshold gate voltage, even at room temperature. We also find that the weighting coefficients a and b (for the inversion and depletion charge densities) strongly depend on the substrate doping and deviate from that reported in the literature. In the case of modulation doped heterostructures, the low-temperature mobility is limited by alloy and Coulomb scattering. Intersubband scattering considerably affects the broadening of the states which, in turn, leads to mobility reduction.			
20. DISTRIBUTION/AVAILABILITY OF ABSTRACT UNCLASSIFIED//UNLIMITED <input checked="" type="checkbox"/> SAME AS RPT. <input type="checkbox"/> DTIC USERS <input type="checkbox"/>		21. ABSTRACT SECURITY CLASSIFICATION Unclassified	
22. NAME OF RESPONSIBLE INDIVIDUAL David K. Ferry		22b. TELEPHONE NUMBER <i>(Include Area Code)</i> (602) 965-2570	22c. OFFICE SYMBOL EE

19960917 138

DTIC QUALITY INSPECTED 2

DISCLAIMER NOTICE



THIS DOCUMENT IS BEST
QUALITY AVAILABLE. THE
COPY FURNISHED TO DTIC
CONTAINED A SIGNIFICANT
NUMBER OF PAGES WHICH DO
NOT REPRODUCE LEGIBLY.

11. Quantum transport: Silicon inversion layers and InAlAs-InGaAs heterostructures.

Quantum transport: Silicon inversion layers and InAlAs-InGaAs heterostructures

D. Vasileska, T. Eldridge,^{a)} and D. K. Ferry

Center for Solid State Electronics Research, Arizona State University, Tempe, Arizona 85287-6206

(Received 21 January 1996; accepted 26 April 1996)

Using a real-time Green's functions formalism, we investigate the influence of depletion charge scattering on the room temperature mobility in scaled silicon metal-oxide-semiconductor field-effect transistors and low-temperature transport in $\text{In}_{0.4}\text{Al}_{0.6}\text{As}$ - $\text{In}_{0.4}\text{Ga}_{0.6}\text{As}$ modulation doped heterostructures. Our simulation results suggest that depletion charge scattering, which is usually ignored, has considerable impact on the electron transport in silicon inversion layers near the threshold gate voltage, even at room temperature. We also find that the weighting coefficients a and b (for the inversion and depletion charge densities) strongly depend on the substrate doping and deviate from that reported in the literature. In the case of modulation doped heterostructures, the low-temperature mobility is limited by alloy and Coulomb scattering. Intersubband scattering considerably affects the broadening of the states which, in turn, leads to mobility reduction.

© 1996 American Vacuum Society

I. INTRODUCTION

Electron transport properties of quasi-two-dimensional (Q2D) systems have been studied quite extensively, experimentally as well as theoretically. The inversion layer at a silicon interface¹ represents the most widely employed physical realization of the Q2D concepts and the electron mobility of the inversion layer electrons is one of the most important parameters for device characterization. It has been confirmed experimentally^{2,3} that for substrates with low doping densities, the electron mobility follows a universal curve when plotted as a function of the effective electric field. However, pushing the devices towards scaling limits⁴ necessarily leads to thinner oxide films (<10 nm) and higher substrate dopings ($>10^{17} \text{ cm}^{-3}$). For these devices, it was recently demonstrated⁵ that experimental mobilities significantly deviate from the universal curves near the threshold voltage as a consequence of significant depletion charge scattering.

Since the invention of the modulation doping technique, transport properties of two-dimensional electron gases in high-mobility modulation doped AlGaAs-GaAs heterojunctions (MDHs) have also been a subject of great interest from both the technological and fundamental point of view.⁶⁻¹⁰ The enhanced mobilities in these structures are attributed to the spatial separation of the electrons from their parent donors, which significantly reduces the scattering rate from the remote impurities.¹¹⁻¹³ This has stimulated much research toward their application in low-power, high-speed devices. Recently, there has been an increased interest devoted to the growth of InAlAs-InGaAs lattice matched heterojunctions¹⁴⁻¹⁶ which have better carrier confinement due to a larger conduction-band discontinuity and a lighter conduction-band effective mass (compared to AlGaAs-GaAs). However, since the electron gas in the InAlAs-

InGaAs MDH is mostly localized within a ternary random alloy (InGaAs), alloy scattering¹⁷ is much more effective so that it is hard to imagine that the low-temperature mobility of InGaAs based modulation doped heterostructures may exceed the very high mobilities already reported in AlGaAs-GaAs heterostructures.

The theoretical model for the calculation of the subband structure and the electron mobilities of the Q2D electron gas, taking into consideration all major scattering mechanisms and both intrasubband and intersubband scattering, is briefly described in Sec. II. In Sec. III, devoted to transport in silicon inversion layers, we describe the influence of depletion charge scattering on the mobility results near the threshold gate voltage. We also show how the weighting coefficients for the inversion and depletion charge densities, which appear in the definition of the average electric field,¹⁸ vary with doping density. Low-temperature transport properties of the modulation doped $\text{In}_{0.4}\text{Al}_{0.6}\text{As}$ - $\text{In}_{0.4}\text{Ga}_{0.6}\text{As}$ heterostructures are discussed in Sec. IV. Some concluding comments related to the present work are given in Sec. V.

II. THEORETICAL MODEL

The subband structure is obtained from a self-consistent solution of the Schrödinger and Poisson equations, coupled with the Dyson equation for the retarded Green's function. Exchange-correlation corrections to the chemical potential are calculated within the local density approximation. The self-energy contributions from the various scattering mechanisms are evaluated by employing the self-consistent Born approximation. Screening is treated within the random phase approximation. In the calculation of the conductivity, we have taken account of a correction term due to the particle-hole ladder diagrams. More details on the calculational model and the analytical expressions for the broadening of the states and conductivity can be found elsewhere.¹⁹

^{a)}Permanent address: McDonnell Douglas Helicopter Systems, 5000 E. McDowell Rd., Mesa, AZ 85215-9797.

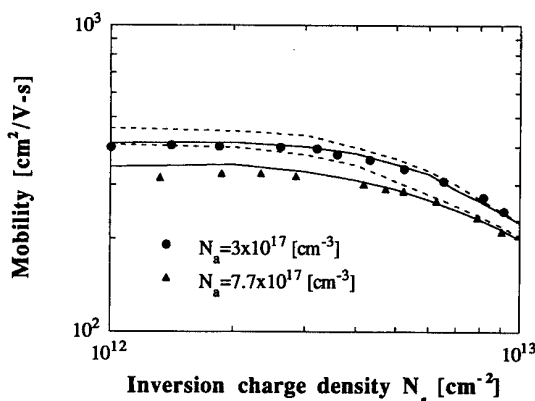


FIG. 1. Room temperature mobility vs inversion charge density for two different devices with high doping densities. For both devices, interface-trap density is $N_{it}=1.75 \times 10^{11} \text{ cm}^{-2}$. We use an exponential model for the surface-roughness autocorrelation function. We find that the rms height of the bumps is 0.26 nm (0.25 nm) for the device with lower (higher) doping. For both devices, roughness correlation length is estimated to be 1.4 nm.

III. SILICON INVERSION LAYERS WITH HIGH DOPING PROFILES

The physical model employed in these calculations includes scattering with all bulk phonons (acoustic and nonpolar optical), surface-roughness scattering, and Coulomb scattering from both ionized impurities in the depletion region and interface/oxide charges. For intervalley scattering (zero-order and first-order interactions), we use the same phonon energies and coupling constants as those relevant for bulk silicon.²⁰ The anisotropy of the deformation potential interaction is also accounted for.²¹ More details about the model can be found in the Appendix.

In Fig. 1, we compare our simulation results for the mobility with the experimental effective mobility data for *n*-channel metal-oxide-semiconductor field-effect transistors (MOSFETs) fabricated on (100) Si wafers. Filled circles and triangles represent the experimental effective mobility data derived from drain conductance measurements.⁵ The inversion charge density has been determined from the gate-channel capacitance measurements. Solid (dashed) lines are the corresponding simulation results when depletion charge scattering is included (omitted) in the calculations. A total of four subbands (three from the unprimed and one from the primed ladder of subbands) are taken into account. We use the real density of states function (DOS) when evaluating the self-consistent potential-energy profile. In contrast to some previous studies,^{18,19,22} we do not ignore the real self-energy corrections (renormalizations of the spectrum) when evaluating the broadening of the states and conductivity. We find that depletion charge scattering leads to mobility reduction of about 9% near the gate voltage thresholds (small values of N_s) for the device with $N_a=3 \times 10^{17} \text{ cm}^{-3}$. For the device with higher substrate doping ($N_a=7.7 \times 10^{17} \text{ cm}^{-3}$), the mobility reduction is about 12.5%. For both devices, the importance of surface-roughness scattering is shifted towards lower gate voltages. In addition, scattering due to acoustic

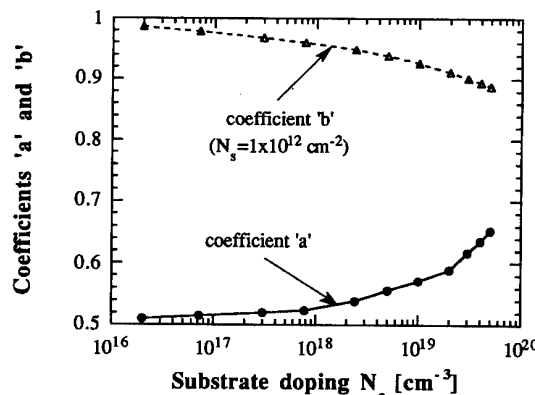


FIG. 2. Variation of the weighting coefficients a and $b=1-\langle z \rangle/W$ with substrate doping. We find that the penetration of the wave functions into the oxide is about 1 nm for very high values of N_a . Slightly higher values for the coefficient b were obtained for $N_s > 1 \times 10^{12} \text{ cm}^{-2}$ (not shown in this figure) due to the closer confinement of the carriers to the interface and increased population of the lower-lying subbands.

and nonpolar optical phonons is found to be of lesser importance in these structures.

It has already been reported^{22,23} that room temperature electron mobilities show universal behavior independent of the substrate doping when plotted as a function of the average electric field $E_{av}=(e/\epsilon_{sc})(aN_s+bN_{depl})$, where a and b are the weighting coefficients for the inversion N_s and depletion N_{depl} charge densities. In Fig. 2 we show the variation of these two coefficients with substrate doping. We find that a significantly deviates from 0.5 for substrates with very high doping densities. We also observe that the weighting coefficient b decreases with increasing substrate doping due to a decrease of the depletion region width. Results shown in Fig. 2 differ from those obtained by Matsumoto and Uemura²⁴ ($a=0.5$ and $b=1$), for example, because in their analytical result for the effective electric field, the terms of the order of $\langle z \rangle/W$ (suggested by Krutsick and White²³), where $\langle z \rangle$ is the centroid of the electron density distribution and W is the depletion region width, were neglected.

IV. In_{0.4}Al_{0.6}As-In_{0.4}Ga_{0.6}As MODULATION DOPED HETEROSTRUCTURES

At low temperatures, the dominant scattering mechanisms in the In_{0.4}Al_{0.6}As-In_{0.4}Ga_{0.6}As MDH shown in Fig. 3 are: remote impurity (from the δ -depletion layer), interface-trap, alloy disorder, interface-roughness and deformation potential, and piezoelectric-coupled acoustic mode scattering.¹² Polar optical phonon scattering is found not to play any significant role at 1.6 K. Screening of the alloy disorder¹⁷ and deformation potential scattering potentials by the free carriers is also neglected because of their short-range nature. This effect should certainly have been included for the long-range electron-piezoelectric acoustic phonon interaction, but since this scattering process is extremely weak at 1.6 K, its matrix element is also left unscreened. Assuming that deformation potential scattering is an elastic process, one has $\hbar\omega_Q/k_B T$

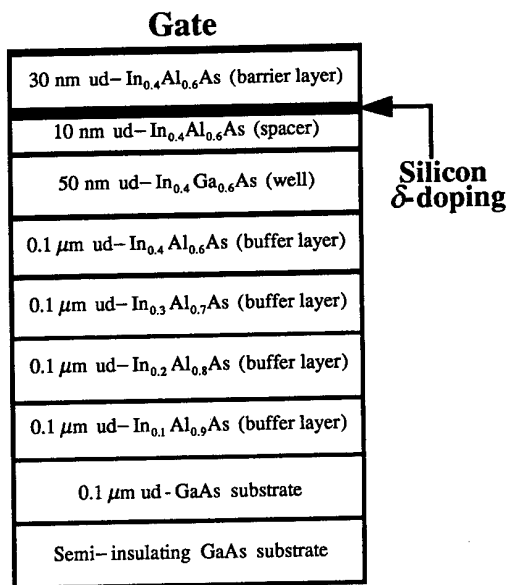


FIG. 3. Cross-sectional view of the δ -doped $\text{In}_{0.4}\text{Al}_{0.6}\text{As}$ - $\text{In}_{0.4}\text{Ga}_{0.6}\text{As}$ heterostructure on (100)-oriented semi-insulating GaAs substrate with intermediate, undoped, and compositionally step-graded buffer layers.

$\approx \sqrt{3c_L m^* / \rho k_B T} = \sqrt{T_e / T}$, where ω_Q is the phonon frequency, k_B is the Boltzmann constant, c_L is the longitudinal elastic constant, m^* is the effective mass, and ρ is the crystal density. Using the material parameters summarized in Table I, we find that the equivalent temperature is $T_e \approx 0.22$ K. Thus, the equipartition approximation can be assumed to hold for temperatures above 1 K for the acoustic mode scattering of thermal electrons. The matrix elements for surface-roughness, acoustic phonon, and alloy disorder scattering can be found elsewhere.²⁶ For the wavevector dependent matrix element for scattering between subband n and m due to Coulomb charges located at a distance $z_i < 0$ from the interface (in the InAlAs layer), we use the following expression:

TABLE I. Values of the $\text{In}_x\text{Ga}_{1-x}\text{As}$ material parameters used in the calculation of the broadening of the states, density of states function, and mobility. For the electron effective mass and static dielectric constants of the $\text{In}_{0.4}\text{Al}_{0.6}\text{As}$, we use $m^* = 0.99 m_0$ and $\epsilon = 11.5 \epsilon_0$, respectively. The energy gaps of strained and unstrained $\text{In}_x\text{Ga}_{1-x}\text{As}$ layers can be found in Ref. 25.

Parameter	Notation and units	Value
Relative electron effective mass	m^*	0.058 for $x=0.4$
Relative static dielectric constant	ϵ	$13.1+1.5x$
Deformation potential constant	D (eV)	8.6–2.8x
Piezoelectric constant	P	0.052–0.007 9x
Longitudinal elastic constant	$c_L (\times 10^6 \text{ N/cm}^2)$	13.97–3.99x
Lattice constant	a (Å)	5.653 25+0.405 15x
Alloy disorder parameter	$\langle V \rangle$ (eV)	0.5–0.55
Crystal density	ρ (g/cm ³)	5.504

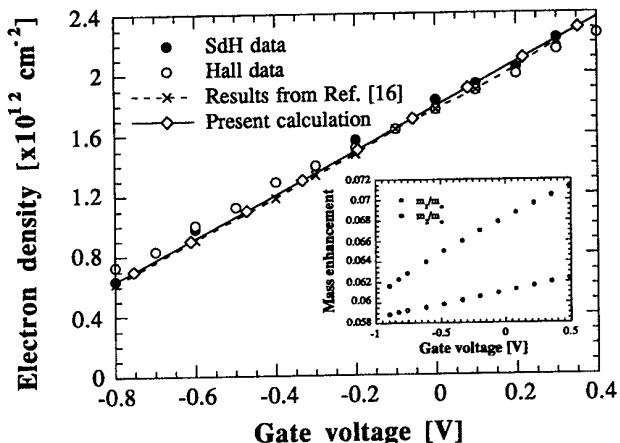


FIG. 4. Gate-voltage dependence of the total electron density for the MDH shown in Fig. 3. Also shown in this figure are the experimental data derived from the low-field Hall and resistivity measurements, Shubnikov–de Haas magnetoresistance measurements as well as the theoretical simulations reported in Ref. 16. The effective mass enhancement due to conduction band nonparabolicity for the carriers residing in the ground and first excited subband is shown in the inset.

$$\langle n | U(q, z_i) | m \rangle = \frac{e^2}{2q\epsilon_b} \int_{-\infty}^0 dz \psi_n(z) \left[e^{-q|z-z_i|} + \frac{\epsilon_b - \epsilon_w}{\epsilon_b + \epsilon_w} e^{-q|z+z_i|} \right] \psi_m(z) + \frac{e^2}{q(\epsilon_b + \epsilon_w)} \int_{-\infty}^0 dz \psi_n(z) e^{-q|z-z_i|} \psi_m(z), \quad (1)$$

in which the image term due to the difference of the static dielectric constants in the well (ϵ_w) and in the barrier layer (ϵ_b) is properly taken into account. The effective mass enhancement with increasing gate voltage due to conduction band nonparabolicity is also taken into account.²⁷

When solving for the subband structure, the number of the self-consistent field iterations was considerably decreased when using the analytical solutions of the Poisson equation. We calculate that in equilibrium, the electron transfer from the δ -doped region to the well (see Fig. 3) is governed by

$$E_F + \Phi_0 - eV_G = \Delta E_c + \frac{e^2 N_D L}{\epsilon_b} - \frac{e^2}{\epsilon_b} \sum_i N_i^b \int_{-\infty}^0 z \psi_i^2(z) dz - \frac{e^2}{\epsilon_b} (W+L) \sum_i \left\{ N_i^w \left[1 - \int_{-\infty}^0 \psi_i^2(z) dz \right] + N_i^b \int_{-\infty}^0 \psi_i^2(z) dz \right\}, \quad (2)$$

where $L = 30$ nm and $W = 10$ nm are the widths of the barrier and spacer layers, E_F is the Fermi level, $\Phi_0 = 0.8$ eV is the Shottky barrier height, V_G is the gate voltage, $\Delta E_c = 0.52$ eV is the conduction band offset, $N_D = 3 \times 10^{12} \text{ cm}^{-2}$ is the Si δ -doping sheet, and $N_i^b (N_i^w)$ is the sheet electron density of the i th subband in the barrier (quantum well).

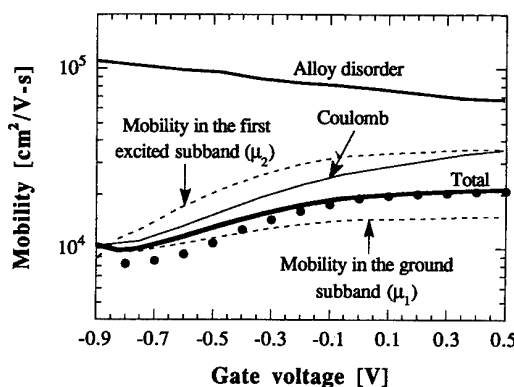


FIG. 5. Cumulative and component theoretical mobilities vs gate voltage. Filled circles are the experimental data determined from Hall effect and resistivity measurements (Ref. 16). The material parameters employed in the simulations are summarized in Table I. Also shown in the figure are the mobilities of the carriers in the ground (μ_1) and first excited subband (μ_2).

Self-consistent results for the gate-voltage dependent electron densities are shown in Fig. 4. We observe good agreement between the experimental data derived from the Hall effect and SdH measurements¹⁶ and the theoretical calculations for all gate voltages. Our simulation results are also in agreement with the theoretical calculations reported by Wieder *et al.*¹⁶ We find that the significant effective mass enhancement (see the inset of Fig. 4) due to conduction band nonparabolicity prevents the population of the third subband until $V_G > 0.4$ V. We also find that, in contrast to silicon inversion layers where exchange-correlation effects are significant even at room temperature, many-body corrections do not considerably affect the subband structure in the MDH because of the small effective mass.

Gate-voltage dependence of the low-temperature theoretical mobilities is shown in Fig. 5. Although the average mobility is $\bar{\mu} = \sum_i N_i \mu_i / N_s$, measured mobilities shown in Fig. 5 are Hall mobilities¹⁶ so that for a multisubband case, the expression $\bar{\mu} = \sum_i N_i \mu_i^2 / \sum_i N_i \mu_i$ is more suitable for comparing the experimental results with the theoretical calculations. To take into account the diffusion effects, the δ -doping sheet is modeled as a 4 nm wide layer centered 8 nm away from the interface with Si doping density of $7.52 \times 10^{18} \text{ cm}^{-3}$. Interface-roughness scattering is assumed to exist at both heterointerfaces of the quantum well. We assume that the rms height of the roughness is one monolayer (ML) ($\Delta = 2.83 \text{ \AA}$). The lateral spread of the interface roughness is taken to be $\zeta = 100 \text{ \AA}$. For this particular heterostructure, we find that surface-roughness and acoustic phonon limited component mobilities (not shown on the figure) are of the order of $(0.5-1) \times 10^6$ and $10^7 \text{ cm}^2/\text{V s}$, respectively. By fitting the calculated mobilities at high gate voltages to the experimental data, we were able to determine the alloy-disorder scattering parameter in the system to be in the range 0.5–0.55. Component mobility results presented in Fig. 5 suggest that the inclusion of alloy scattering, in addition to Coulomb scattering (from the ionized donors in the δ -doped region and

interface traps), leads to good agreement between the theoretical calculations and the experimental data. The dip in the theoretical mobility at $V_G = -0.85$ V signals that a new channel (second subband) for scattering opens in the MDH which leads to a sudden increase in phase space for scattering between the two subbands to occur. Since the carriers residing in the first excited subband are at about four times larger average distance from the heterointerface (compared to those in the ground subband), they do not feel as much the Coulomb scattering potentials and exhibit about two times higher mobility.

V. CONCLUSIONS

Our results suggest that depletion charge scattering, which has been ignored in some previous theoretical studies, is responsible for the deviation of the mobility from the universal curves near the threshold voltage. At high gate voltages (high values of N_s), due to the closer confinement of the carriers to the interface, the magnitude of the mobility in these highly doped samples is considerably reduced by surface-roughness scattering, in addition to the still significant intervalley scattering. We also find that the weighting coefficients a and b —that appear in the definition of the average electric field—show a pronounced doping dependence. For the $\text{In}_{0.4}\text{Al}_{0.6}\text{As}-\text{In}_{0.4}\text{Ga}_{0.6}\text{As}$ MDH, we find that at $T = 1.6$ K the magnitude of the mobility is limited by Coulomb and alloy scattering. From the subband structure (gate-voltage dependence of the electron density) and mobility simulations, we calculate that the relevant effective mass at the conduction band minima of the $\text{In}_{0.4}\text{Ga}_{0.6}\text{As}$ ternary alloy is $m^* = 0.058 m_0$. An observed effective mass enhancement suggests that nonparabolicity effects are considerable in this MDH and must be taken into account if accurate mobility results are desired. The effect of the many-body interactions, calculated in the local density-functional approximation, is found not to be important for the MDH.

ACKNOWLEDGMENTS

The authors would like to acknowledge the Office of Naval Research for sponsoring this project. They also would like to thank H. H. Wieder for providing us with valuable information about the material parameters of the $\text{In}_{0.4}\text{Al}_{0.6}\text{As}-\text{In}_{0.4}\text{Ga}_{0.6}\text{As}$ heterostructure.

APPENDIX

The expression for the matrix elements for scattering between subbands n and m due to a Coulomb charge in the depletion region, in the oxide, or right at the interface, in the presence of a different dielectric medium, can be found in the review article by Ando, Fowler, and Stern.¹ For the surface-roughness matrix element, we use the result obtained by Ando²⁸ who corrected the result obtained by Matsumoto and Uemura²⁴ by taking into account the change in the electron density distribution and the effective dipole moment of

the deformed Si–SiO₂ surface in addition to the usual local potential energy term that equals the linear term of the Taylor expansion of the surface potential.

For anisotropic elastic continuum such as silicon, for which the deformation potential constant Ξ is a tensor,²⁹ matrix element squared for scattering between subbands n and m due to acoustic phonons, in the usual equipartition approximation, equals to²¹

$$|\langle n|U_{\lambda}^{ac}(\mathbf{q})|m\rangle|^2 = \frac{k_B T}{\rho V \nu_{s\lambda}^2} [\Delta_{\lambda, nm}^{\text{eff}}(\mathbf{q})]^2 F_{nm}, \quad (\text{A1})$$

where

$$F_{nm} = \int_0^{\infty} dz \psi_n^2(z) \psi_m^2(z), \quad (\text{A2})$$

$\nu_{s\lambda}$ is the sound velocity, and ρ is the Si mass density. The effective deformation potential constant that appears in expression (A1) is calculated from

$$[\Delta_{\lambda, nm}^{\text{eff}}(\mathbf{q})]^2 = \frac{1}{F_{nm}} \int_0^{\infty} dq_z \Delta_{\lambda}^2(\theta_Q) |\mathcal{F}_{nm}(q_z)|^2, \quad (\text{A3})$$

where

$$\mathcal{F}_{nm}(q_z) = \int_0^{\infty} dz \psi_n(z) e^{iq_z z} \psi_m(z) \quad (\text{A4})$$

and θ_Q is the angle between the wave vector \mathbf{Q} of the emitted (absorbed) phonon and the longitudinal axis of the valley. According to Herring and Vogt,²⁹ the effective deformation potentials $\Delta_{\lambda}(\theta_Q)$ ($\lambda = \text{LA or TA}$) that appear in Eq. (A3) are given by

$$\Delta_{\text{LA}}(\theta_Q) \approx \Xi_d + \Xi_u \cos^2(\theta_Q) \quad (\text{A5a})$$

and

$$\Delta_{\text{TA}}(\theta_Q) \approx \Xi_u \cos(\theta_Q) \sin(\theta_Q). \quad (\text{A5b})$$

In Eqs. (A5a) and (A5b), Ξ_u is the uniaxial shear potential, and Ξ_d is the dilatation potential that are believed to have values of approximately 9.0 and -11.7 eV, respectively.^{21,30} It is important to point out that Eq. (A5b) accounts for the contribution of both TA branches.

The matrix element for nonpolar optical phonon scattering is generally found from a deformable ion model. The zero-order process, which describes a perturbation that can be associated with the local dilatation or compression of the lattice which produces local fluctuation in the electron energy, dominates at moderately high electron energies. The matrix elements for scattering between subbands n and m (that belong to α and β valleys) due to this zero-order interaction is given by

$$|\langle n|U_{\lambda}^{\text{op}(0)}|m\rangle|^2 = \frac{\hbar D_{\lambda}^2}{2\rho V \omega_{o\lambda}} F_{nm}, \quad (\text{A6})$$

where D_{λ} is the deformation field and $\omega_{o\lambda}$ is the frequency of the phonon mode.

When the zero-order matrix element for the optical or intervalley interaction vanishes, then D_{λ} is identically zero.

In this case, one has to consider the first-order term of the interaction. The squared matrix element for scattering between subbands n (α valley) and m (β valley) due to this first-order process is given by³¹

$$|\langle n|U_{\lambda}^{\text{op}(1)}|m\rangle|^2 = \frac{\hbar D_{1\lambda}^2}{2\rho V \omega_{o\lambda}} (q^2 F_{nm} + c_{nm}), \quad (\text{A7})$$

where

$$c_{nm} = \int_0^{\infty} dz \left\{ \frac{d}{dz} [\psi_n(z) \psi_m(z)] \right\}^2. \quad (\text{A8})$$

In the scattering among the equivalent valleys, there are two types of phonons that might be involved in the process. The first type, the so-called g phonon couples the two valleys along opposite ends of the same axis, i.e., $\langle 100 \rangle$ to $\langle 100 \rangle$. This is an umklapp process and has a net phonon wavevector $0.3\pi/a$. The so-called f phonons couple the $\langle 100 \rangle$ valley with $\langle 010 \rangle$, $\langle 001 \rangle$, etc. Hence, the reciprocal lattice vector involved in the g -process is \mathbf{G}_{100} and that for an f process is \mathbf{G}_{111} .

Within a four subband approximation, scattering between the two valleys in the ϵ_0 , ϵ_1 , and ϵ_2 subbands involves only g -type phonons. The scattering between these three minima is treated by using a high-energy phonon of 750 K activation temperature (treated as zero-order interaction) and 134 K phonon treated via first order interaction. Scattering between the ϵ_0 , ϵ_1 , and ϵ_2 subbands and the four ϵ'_0 subbands involves f phonons with activation temperatures of 630 and 230 K treated via zero-order and first-order interaction, respectively. Scattering between the ϵ'_0 subbands involves both g and f phonons with activation temperatures of 630 K (zero-order interaction) and 190 K (first-order interaction). All of the high-energy phonons are assumed to be coupled with a value of $D_{\lambda} = 9 \times 10^8$ eV/cm, and all of the first-order coupled phonons are assumed to be coupled with $D_{1\lambda} = 5.6$ eV. These values are consistent with the results given in Refs. 20 and 32.

¹T. Ando, A. B. Fowler, and F. Stern, Rev. Mod. Phys. **54**, 437 (1982).

²A. G. Sabinis and J. T. Clemens, IEDM Tech. Dig. **18** (1979).

³S. C. Sun and J. D. Plummer, IEEE Trans. Electron Devices **ED-27**, 1497 (1980).

⁴M. Ono, M. Saito, T. Yoshitomi, C. Fiegna, T. Ohguro, and H. Iwai, IEEE Trans. Electron Devices **ED-42**, 1822 (1995).

⁵S. Takagi, A. Toriumi, M. Iwase, and H. Tango, IEEE Trans. Electron Devices **ED-41**, 2357 (1994).

⁶R. Dingle, H. L. Störmer, A. C. Gossard, and W. Wiegmann, Appl. Phys. Lett. **33**, 665 (1978).

⁷H. L. Störmer, A. Pinczuk, A. C. Gossard, and W. Wiegmann, Appl. Phys. Lett. **38**, 691 (1981).

⁸A. Kastalsky, R. Dingle, K. Y. Cheng, and A. Y. Cho, Appl. Phys. Lett. **41**, 274 (1982).

⁹K. Lee, M. S. Shur, T. J. Drummond, and H. Morkoç, J. Appl. Phys. **54**, 6432 (1983).

¹⁰L. Pfeiffer, K. W. West, H. L. Störmer, and K. W. Baldwin, Appl. Phys. Lett. **55**, 1888 (1989).

¹¹E. E. Mendez, P. J. Price, and M. Heiblum, Appl. Phys. Lett. **45**, 294 (1984).

¹²H. L. Störmer, Surf. Sci. **132**, 519 (1983).

¹³P. J. Price, Surf. Sci. **143**, 145 (1984).

¹⁴N. C. Tien, J. Chen, J. M. Fernández, and H. H. Wieder, IEEE Trans. Electron Device Lett. **EDL-13**, 621 (1992).

¹⁵J. Chen, H. H. Wieder, and A. P. Young, *J. Appl. Phys.* **76**, 4743 (1994).

¹⁶H. H. Wieder, R. S. Goldman, J. Chen, and A. P. Young, *J. Vac. Sci. Technol. B* **13**, 1853 (1995).

¹⁷G. Bastard, *Appl. Phys. Lett.* **43**, 591 (1983).

¹⁸D. Vasileska, P. Bordone, T. Eldridge, and D. K. Ferry, *J. Vac. Sci. Technol. B* **13**, 1841 (1995).

¹⁹D. Vasileska, T. Eldridge, P. Bordone, and D. K. Ferry, VLSI Design (to be published).

²⁰D. K. Ferry, *Phys. Rev. B* **14**, 1605 (1976).

²¹M. V. Fischetti and S. E. Laux, *Phys. Rev. B* **48**, 2244 (1993).

²²D. Vasileska, P. Bordone, T. Eldridge, and D. K. Ferry, *Physica B* (to be published).

²³T. J. Krutsick and M. H. White, *IEEE Trans. Electron Devices* **ED-35**, 1153 (1988).

²⁴Y. Matsumoto and Y. Uemura, *Jpn. J. Appl. Phys. Suppl.* **2**, 367 (1974).

²⁵S. Adachi, *J. Appl. Phys.* **53**, 8775 (1982).

²⁶S. M. Goodnick and D. K. Ferry, in *Physics and Chemistry of III-V Compound Semiconductor Interfaces*, edited by C. W. Wilmsen (Plenum, New York, 1985).

²⁷E. O. Kane, *J. Phys. Chem. Solids* **1**, 249 (1957); in *Semiconductors and Semimetals*, edited by R. K. Willardson and A. C. Beer (Academic, New York, 1966), p. 75; in *Handbook on Semiconductors*, edited by W. Paul (North-Holland, Amsterdam, 1982), Vol. 1, p. 193.

²⁸T. Ando, *J. Phys. Soc. Jpn.* **43**, 1616 (1977).

²⁹C. Herring and E. Vogt, *Phys. Rev.* **101**, 944 (1956).

³⁰B. K. Ridley, *Quantum Processes in Semiconductors* (Oxford University Press, New York, 1993).

³¹D. K. Ferry, *Semiconductors* (Macmillan, New York, 1991).

³²D. K. Ferry, *Phys. Rev. B* **14**, 5364 (1976).